Design of a loading system for cyclic test on sutured organs

The International Journal of Advanced Manufacturing Technology
https://doi.org/10.1007/s00170-025-16924-7

ORIGINAL ARTICLE

Friction stir welding of additively manufactured CuNiSiCr: effect of post-weld heat treatments on microstructure and mechanical properties

Mohammad Abankar[1] · **Vincenzo Lunetto**[1,2] · **Pasquale Russo Spena**[1,2]

Received: 7 May 2025 / Accepted: 1 November 2025

Abstract
This study investigates the friction stir welding (FSW) of a CuNiSiCr alloy produced by laser powder bed fusion and the role of post-weld heat treatments in the microstructural evolution and mechanical performance of welded joints. The as-built alloy exhibited columnar grains, porosity, and lack-of-fusion defects. FSW refined the microstructure within the stir zone (SZ) and dramatically reduced porosity, both in pore number and size, as revealed by X-ray tomography. Mechanical testing showed that FSW joints outperformed the as-built specimens, with increased yield and tensile strengths, albeit with reduced ductility. Aging at 500 °C markedly enhanced hardness across both the base material and the SZ, achieving peak values of about 195 HV after 2 h. Peak-aged joints reached yield and tensile strengths that were 17% and 16% higher, respectively, than those of the base alloy. Direct aging proved as effective as conventional solution treatment and aging, simplifying the heat treatment route. These findings show that FSW followed by direct aging offers a promising approach for obtaining high-performance joints, providing a viable pathway for producing large, complex, additively manufactured CuNiSiCr assemblies with improved structural integrity.

Keywords Friction stir welding · CuNiSiCr · Laser powder bed fusion · Additive manufacturing · Aging heat treatment

1 Introduction

Copper is a versatile metal that is known for its excellent thermal and electrical conductivity, corrosion resistance, and good machinability [1–4]. These properties make copper and its alloys valuable for several applications, such as in the automotive, aerospace, and electrical industries [5–7]. They are widely used in components such as heat sinks, radiators, nozzles, industrial electrode plates, large motor rotors, high pulse magnetic field conductors, and induction heating coils [4, 8, 9]. Heat exchangers are designed with high surface-to-volume ratios and intricate geometries (e.g., thin fins and tubes) to maximize the heat transfer area and reduce turbulence [10–12]. Induction heating coils are manufactured in different shapes and sizes to ensure well-distributed electromagnetic fields for targeted heating [12]. Traditional production methods often struggle to realize such complex geometries efficiently, in terms of cost and time [4, 13, 14]. However, advancements in 3D printing technology have enabled the fabrication of intricate copper-based parts, thereby overcoming conventional design limitations [4, 6, 15]. Among the various AM technologies, powder bed fusion (PBF) is the most widely used for the fabrication of copper-based components. PBF is categorized as laser powder bed fusion (LPBF) or electron beam powder bed fusion (EB-PBF) depending on the heating source. Although EB-PBF is generally preferred for pure copper, due to its ability to minimize reflectivity, prevent oxidation, and maximize energy absorption, without requiring preheating to increase the component density [4, 6], it presents certain challenges, such as high costs and lower geometrical accuracy [4, 16]. Although exhibiting reduced

✉ Mohammad Abankar
mohammad.abankar@polito.it

[1] Department of Management and Production Engineering, Politecnico di Torino, Corso Duca degli Abruzzi 24, Torino 10129, Italy

[2] Advanced Joining Technologies Laboratory (J-Tech@PoliTO), Politecnico di Torino, Corso Duca degli Abruzzi 24, Torino 10129, Italy

Published online: 20 November 2025

thermal and electrical conductivity due to the presence of alloying elements such as Ni, Si, or Cr [17, 18], LPBF is more commonly used for copper alloys since it offers superior mechanical strength and enhanced processability [19–27]. CuNiSi is one of the most widely used copper-based alloys produced via LPBF. It is a heat-treatable copper alloy that combines relatively high thermal and electrical conductivity with increased strength [28–30]. Several studies [28–30] have investigated the LPBF processability and resulting properties of CuNiSi alloys, while others [31–34] have concentrated on the effects of aging heat treatments on both electrical and thermal conductivity. Precipitation hardening treatments typically involve a solution treatment at temperatures between 760 and 955 °C, followed by aging at 260 to 565 °C for different durations, depending on the composition and the desired mechanical properties of the alloy [35]. Optimized solution and aging treatments have been shown to significantly improve the mechanical strength and hardness of this alloy [26, 31–34]. The primary strengthening mechanism has been attributed to the precipitation of coherent nickel-silicon phases, such as the δ-Ni_2Si phase [33]. These heat treatments also have a beneficial effect on electrical conductivity, which can increase from initial values as low as 10 to 40% IACS, depending on the thermal cycle applied [34, 36, 37].

AM CuNi2SiCr is an enhanced variant of the CuNiSi alloy, which was specifically developed to improve corrosion and wear resistance through the addition of chromium. Apart from these benefits, chromium also increases stiffness at elevated temperatures [38, 39], thus making CuNi2SiCr particularly suitable for demanding applications, such as heat sinks, where efficient thermal management is essential to prevent system overheating. Several studies [40–42] have shown that the addition of chromium improves the mechanical properties of CuNiSi alloys and has a minimal negative impact on electrical conductivity [32]. This effect is largely due to the low solubility of chromium in the copper matrix (~ 0.1 at.% at 510 °C and ~ 0.3 at.% at 930 °C) [17, 43]. In addition, chromium promotes the formation of Cr-based precipitates that contribute to the development of a compact passivation film, thereby improving corrosion resistance [44, 45]. The presence of Cr_3Si phases also helps stabilize the microstructure of the alloy and maintain the mechanical properties of CuNiSiCr at high temperatures, even beyond the dissolution point of nickel silicide precipitates [40, 46]. Wu et al. [46] investigated the effects of annealing and peak aging on this copper alloy. They found that solid-solution scattering and the Orowan strengthening were the main mechanisms that affected the electrical and mechanical properties. Similarly, Wang et al. [17] studied how solution treatment and aging influence the mechanical properties of a CuNiSiCr alloy produced via powder metallurgy. They obtained a tensile strength of 820 MPa and a thermal conductivity of 110 W/(m·K).

The outstanding properties of the CuNiSiCr alloy, combined with the design flexibility offered by additive manufacturing, have made its use widespread in advanced engineering applications. However, producing the large components that are often required in electrical and thermal systems present some challenges, including higher production costs, extended fabrication times, and an increased risk of defects during the layer-by-layer fabrication process [47]. Moreover, AM parts frequently need to be assembled into large structures, thus making effective and reliable welding techniques critical for the structural integrity of such structures [48]. Despite this, research into the weldability and structural performance of joints in AM copper alloys remains somewhat limited.

Friction stir welding (FSW) is a solid-state welding technique that offers several promising solutions. It enables the creation of strong, permanent joints with minimal deformations and residual stresses. FSW is not only cost-effective and easily automatable but also overcomes many of the limitations of fusion welding, particularly for materials with high thermal conductivity like copper. FSW has already been successfully applied to bulk copper components on an industrial scale for the production of heat exchangers, liquid cold plates, containment canisters for nuclear waste, and backing plates for sputtering equipment [49]. FSW offers several advantages over traditional fusion welding, such as the minimization of weld porosity, the formation of fine microstructures with improved strength [50–53], and the mitigation of such issues as excessive heat input, oxidation, and wide heat-affected zones (HAZs). These benefits make FSW a suitable and promising technique for joining AM copper alloys, including CuNiSiCr [54–60]. Additionally, post-weld heat treatments on FSW joints can be employed to further improve the mechanical properties of heat-treatable alloys and their joints [48].

This study investigates the butt FSW of a CuNiSiCr alloy fabricated by LPBF, with a focus on its effects on the porosity, precipitation hardening, and mechanical performance of the resulting joints. In addition, the combined influence of FSW and subsequent post-weld heat treatments on the microstructural and mechanical properties of the welded joints has been assessed. Since the strength of CuNiSiCr primarily depends on precipitation hardening, understanding how welding-induced thermal cycles interact with any subsequent heat treatments is essential for preserving or enhancing its mechanical properties. Through the development of a processing-structure-property relationship, this study aims to provide valuable insights into the optimization of FSW joining strategies and subsequent post-weld thermal treatments for AM CuNiSiCr.

Table 1 Chemical composition (wt.%) of the CuNiSiCr alloy according to the supplier technical datasheet

	Chemical Composition wt%				
CuNiSiCr	**Cu**	**Ni**	**Si**	**Cr**	**Fe**
	Bal.	2–3	0.5–0.8	0.2–0.5	0.15

2 Materials and methods

2.1 Additive manufacturing

Four mm thick CuNiSiCr plates, measuring 75 × 55 mm, were manufactured using LPBF. The chemical composition of the CuNiSiCr powder used in the experiment is detailed in Table 1. The key parameters for the printing process included a laser power of 370 W and a layer thickness of 30 µm. The fabricated samples had an average density of 94 ± 1.5%. All the samples were printed with their 75 mm lengths oriented parallel to the build direction to ensure consistency in material properties.

2.2 Friction stir welding

Single-pass friction stir butt welding was performed on CuNiSiCr plates using an FSW machine (Stirtec GmbH, mod. FSW100) equipped with a water-cooled spindle, as schematically illustrated in Fig. 1a). The FSW tool, made of a WRe alloy (75 wt% W + 25 wt% Re), was selected to withstand the high temperatures generated during the welding process (see Fig. 1b). It featured a truncated cone pin with a threaded surface and a flat scrolled shoulder, and it was specifically designed to enhance material flow and break the superficial oxide layers, which are typically present in Cu-based alloys. A preliminary experimental campaign was conducted to identify the optimal process parameters, which were found to be as follows: 900 rpm rotational speed, 100 mm/min welding speed, 2 ° tilt angle, 3.9 mm plunge depth, 10 mm/min plunge speed, and 2 s dwell time. Argon shielding gas was supplied through two nozzles, which were positioned at the front and rear of the FSW tool, to prevent oxidation during welding.

2.3 Post-process heat treatments

Precipitation hardening copper alloys generally undergo a solution treatment followed by aging to enhance their hardness and strength. However, the solution treatment completely disrupts the ultrafine microstructure and the high solute supersaturation achieved through the LPBF process, thereby potentially reducing the beneficial effects [61]. Direct aging (i.e., aging without a prior solution treatment) can be adopted after LPBF to preserve these benefits, leading to strength enhancement through precipitation hardening while maintaining a fine microstructure.

In this work, both the as-built CuNiSiCr and the FSW joints underwent aging heat treatments to enahnce their strength through the precipitation of second phases, such as NiSi and Cr_3Si [33, 62]. Two distinct heat treatment routes were employed at a heating rate of 10 °C/min, as illustrated in Fig. 2:

- Direct aging (*DA*): samples were directly aged at 500 °C for 1 to 16 h, followed by air cooling. These samples were labeled *DAy*, where y denotes the specific aging duration
- T6 (*ST*): an initial solution treatment at 900 °C for 2 h, followed by water quenching at room temperature. The samples were aged at 500 °C for 1 to 16 h, and then underwent final air cooling.

2.4 Microstructural and structural analysis

The metallographic sample preparation followed a standard procedure that involved grinding, polishing, and final

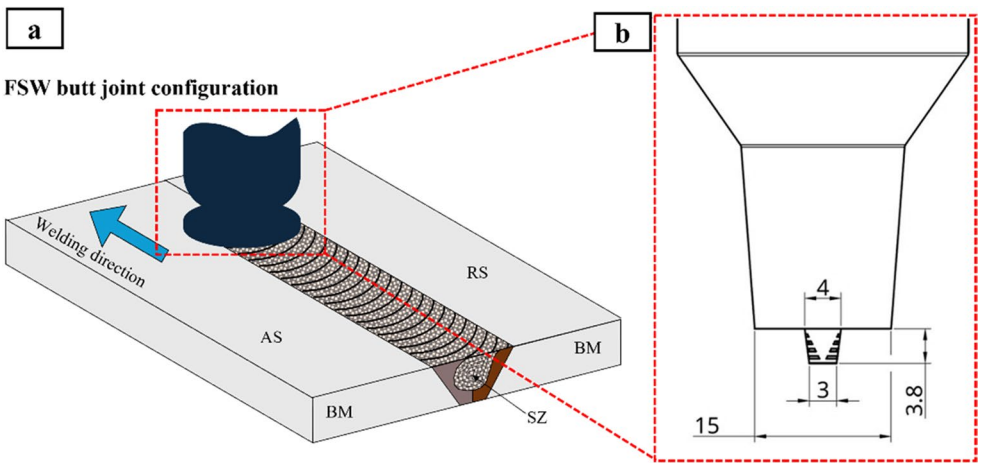

Fig. 1 (**a**) Schematic of the FSW process and (**b**) geometry of the tool used for the welding tests (dimensions in [mm])

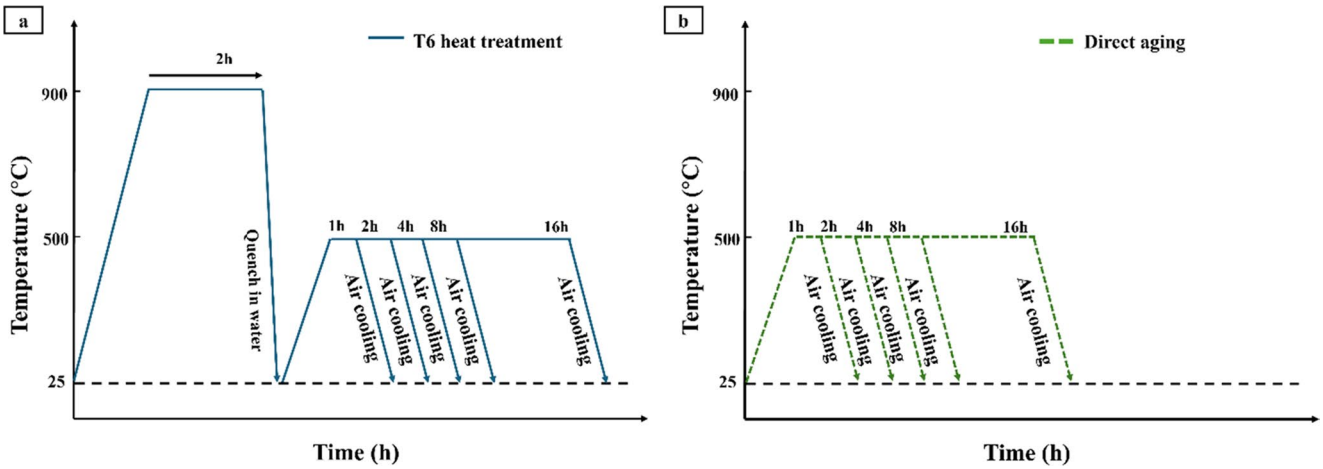

Fig. 2 Schematic representation of (**a**) the T6 and (**b**) the direct aging heat treatments applied to the AM CuNiSiCr in both the as-built and FSW-welded conditions

chemical etching. The etching solution consisted of 5 g $FeCl_3$, 50 ml HCl, and 100 ml distilled water. Microstructural and fractographic analyses were conducted using a field-emission scanning electron microscope, FE-SEM (Tesca, mod. MIRA3). In addition, elemental mapping was obtained using X-ray energy dispersive spectroscopy (EDS) integrated with the FE-SEM. X-ray diffraction (XRD) was carried out on the base material (BM), the stir zone (SZ) of the FSW joints, and both regions under peak-aged conditions (aging at 500 °C for 2 h) for phase analysis, using a Bourevestnik Dron-8 diffractometer with Cu Kα radiation (wavelength λ = 1.5428 Å).

2.5 Mechanical testing

Five dogbone tensile samples were extracted from each welded coupon using wire electrical discharge machining (Baoma, mod. BMW-3000) for mechanical testing, along with additional samples prepared for microstructural examination, as illustrated in Fig. 3. The surfaces of the tensile specimens were machined by milling to remove any superficial effects resulting from wire electrical discharge machining (surface roughness) and heat treatments (oxidation). Tensile testing (ZwickRoell, mod. Z050) was carried out on the as-built and FSW joints in both heat-treated and non-heat-treated conditions, in accordance with the ISO 6892 standard [63], at a crosshead speed of 10 mm/min. A 10 mm buffer zone was maintained at both ends of the joint to ensure that the extracted specimens were unaffected by any local variations in the mechanical properties near the joint boundaries. Hardness testing was performed on as-built and welded joints under both heat-treated and non-heat-treated conditions using Vickers hardness measurements (Innovatest, mod. Nova 130), in accordance with the ISO 6507 standard [64]. Tests were conducted with a 500 g load and a 15 s dwell time. A hardness map of the welded joint was generated by placing indentations 1 mm apart across the cross-section to provide a detailed assessment of the hardness distribution.

3 Results and discussion

3.1 Microstructure of the as-built and joint samples

Figure 4a) shows an optical micrograph of the CuNiSiCr alloy after LPBF (i.e., as-built). The microstructure is primarily composed of coarse columnar grains, together with a smaller fraction of equiaxed grains, with grain sizes ranging from approximately 2 to 90 µm. The columnar grains result from epitaxial growth induced by the successive laser passes during the layer-by-layer fabrication process. Metallographic examination revealed significant porosity in the CuNiSiCr alloy, which led to a reduction in its relative density. The presence of columnar grains and diffuse porosity are well-documented issues in laser-based AM of copper and its alloys [65], high-entropy alloys [66], and magnesium alloys [67]. Porosity represents a lack of fusion (LOF) defect, as shown in Fig. 4b), characterized by partially melted or unmelted powder particles caused by insufficient energy input during processing, which prevented complete melting and proper bonding between layers [68]. LOF defects are more critical in copper-based AM alloys than in aluminum ones and are commonly attributed to two main factors that hinder powder melting: (a) high thermal conductivity (~ 400 W/(m·K), compared to ~ 240 W/(m·K) for aluminum alloys), which promotes rapid heat dissipation from the melt pool to the surrounding material [4] and (b) high laser reflectivity, which reduces laser energy absorption [69].

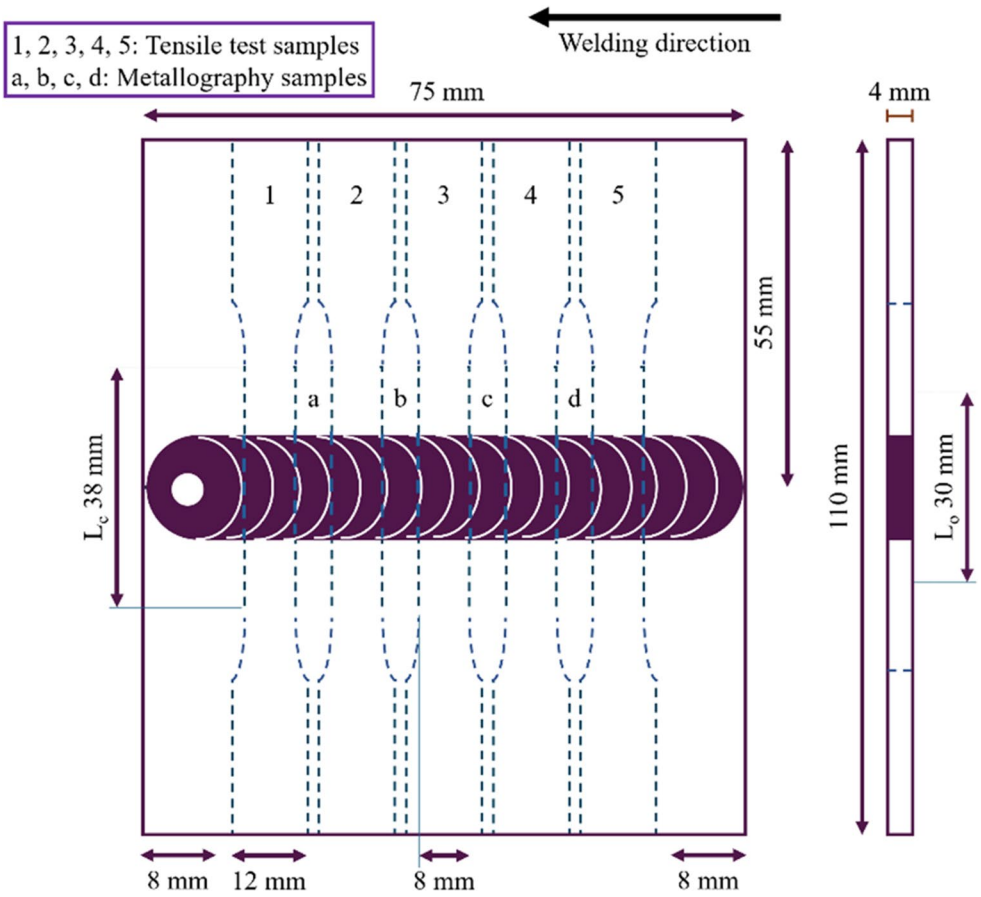

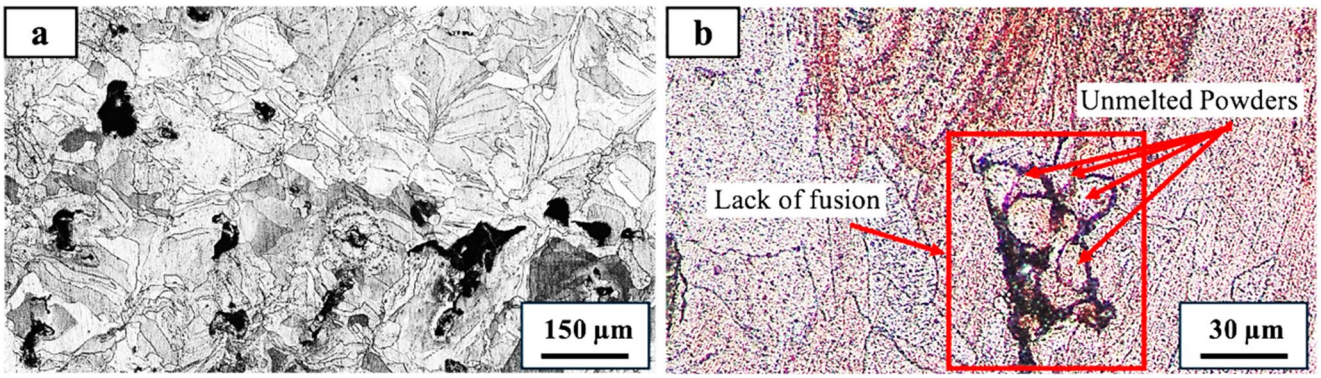

Fig. 3 Sketch of the FSW welds and the locations of the tensile and metallographic samples

Fig. 4 Optical microscopy images of (**a**) as-built CuNiSiCr and (**b**) a LOF defect containing unmelted powders

Figure 5 illustrates an example of an EDS map obtained from an LOF region. The elemental distribution reveals that copper, nickel, and chromium are homogeneously dispersed throughout the microstructure, with no evidence of elemental segregation. Conversely, silicon exhibits localized enrichment in areas where oxygen is also detected, suggesting the formation of SiO_2. This oxidation likely originated from residual oxygen within the powder and/or exposure to atmospheric oxygen during processing. Indeed, copper powders are highly susceptible to oxidation during storage and handling, making a certain degree of surface oxidation almost unavoidable [4]. Such localized oxidation can inhibit complete melting of the powder and may therefore contribute to the formation of LOF defects.

Figure 6a) shows a micrograph of the cross-section of an FSW joint. The microstructure within the weld zone differs notably from that of the as-built CuNiSiCr alloy. The SZ features a refined microstructure resulting from the intense

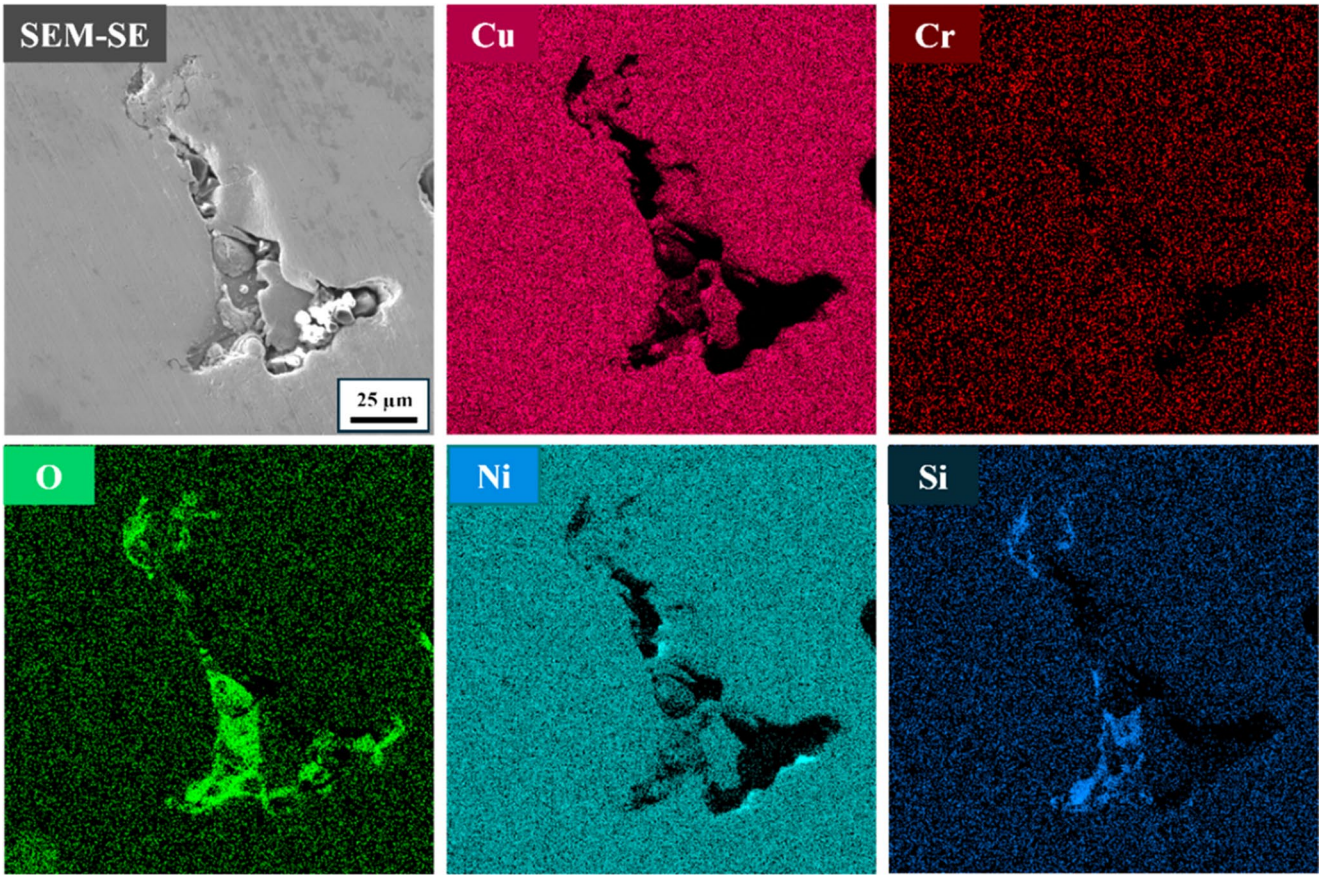

Fig. 5 EDS maps of a LOF defect in the AM CuNiSiCr alloy

mechanical stirring by the rotating tool, combined with recrystallization induced by the high heat input and severe plastic deformation during the FSW process [70]. The weld zone broadens toward the upper surface, reflecting greater heat generation and enhanced material flow beneath the tool shoulder. A clearly defined boundary marks the edges of the SZ on both the retreating side (RS) and the advancing side (AS), emphasizing microstructural heterogeinity across the

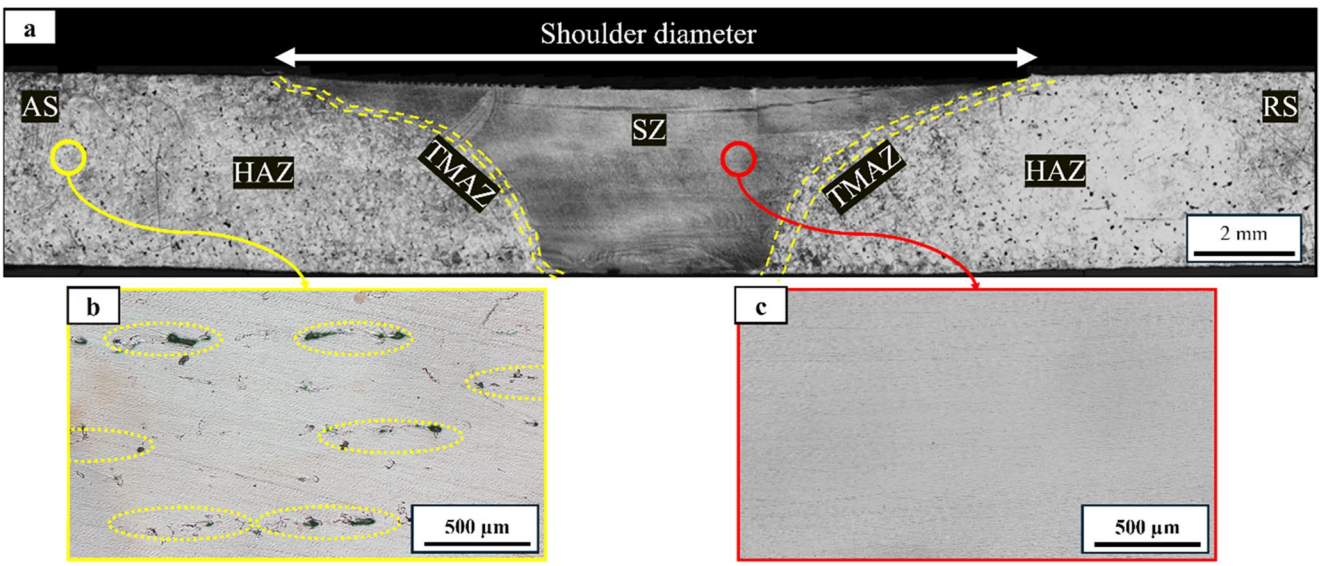

Fig. 6 Microstructures of a CuNiSiCr FSW joint: (**a**) macroscopic cross-section, (**b**) unetched microstructure of CuNiSiCr and of (**c**) the SZ

welded joint. A comparison between the unetched microstructures of the CuNiSiCr alloy and the FSW joint reveals the effectiveness of the tool stirring action in reducing the intrinsic porosity of the LPBF microstructure. As shown in Fig. 6b), the as-built CuNiSiCr exhibits a relatively uniform distribution of porosity, a feature commonly observed in AM copper components. However, this porosity is largely eliminated within the SZ because of the intense stirring action. These findings underscore the beneficial role of FSW in mitigating one of the most common defects in copper-based parts produced by LPBF.

Figure 7 provides a detailed view of the different regions within the welded joints, including the SZ, the thermomechanically affected zone (TMAZ), and the HAZ. Figure 7a) shows the transition region between the SZ and the HAZ on the advancing side. The TMAZ is not visible at this low magnification due to its limited extent. The SZ exhibits distinct metal flow patterns caused by the stirring action of the FSW tool, whereas the adjacent HAZ retains features of the as-built material. This indicates that the portion of the HAZ closest to the SZ did not reach the recrystallization temperature. Figure 7b), which shows a higher magnification of this region, reveals the TMAZ, approximately 100 µm wide. This region experienced mechanical deformation; therefore, the TMAZ features elongated grains aligned in the material flow direction. Figure 7c) displays the interface between the SZ and the HAZ on the retreating side, while a higher magnification of this area is provided in Fig. 7d). A comparison between Figs. 7b) and 7 d) shows that the transition from the HAZ to the SZ is more gradual on the retreating side than on the advancing side. This observation is consistent with the findings of Moeini et al. [70], who reported a smoother transition on the retreating side during FSW of an AlSi10Mg alloy produced via LPBF. This asymmetry is attributed to the characteristic material flow during FSW, where the stirred material moves from the retreating side to the advancing side before being forced downward into the bottom regions of the weld on the advancing side [71]. Figure 7e) depicts the microstructure of the SZ, which consists of ultrafine grains with an average size of about 5 µm, significantly smaller than those in the BM (see Fig. 4a)). Finally, Fig. 7f) displays an optical micrograph of the HAZ region, which retains a microstructure similar to that of the BM, showing only minor grain coarsening, with grain sizes ranging from approximately 2 to 115 µm.

3.2 Porosity evaluation through 3D X-ray computed tomography

Figure 8 shows a 3D visualization of the pores within and around the CuNiSiCr FSW joints, as obtained through X-ray computed tomography. Two regions of interest

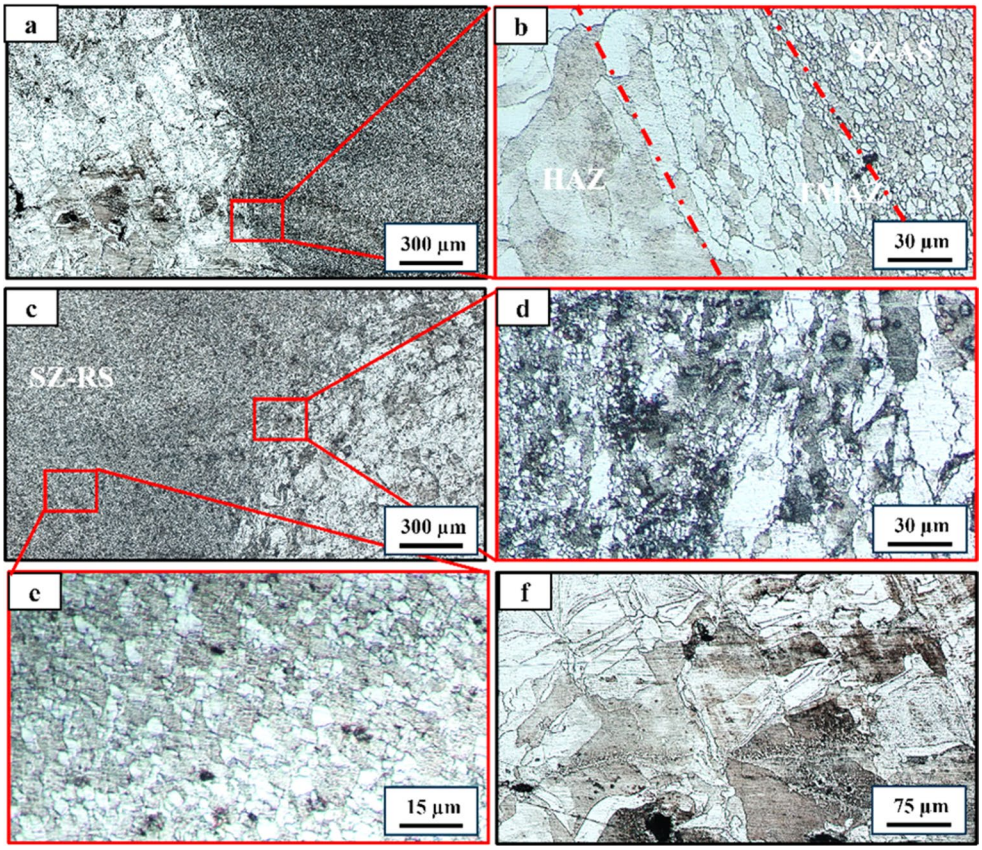

Fig. 7 Microstructures of different regions in an FSW joint of the AM CuNiSiCr: (**a**) low- and (**b**) high-magnification images of the transition region between the SZ and the HAZ on the advancing side; (**c**) low- and (**d**) high-magnification images of the transition region between the SZ and the HAZ on the retreating side; (**e**) SZ and (f) HAZ microstructures

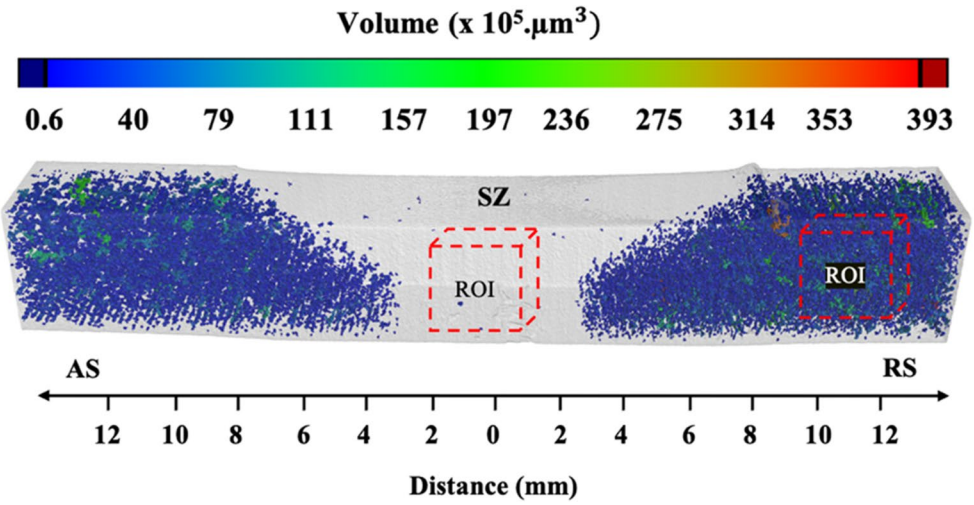

Fig. 8 Pore distribution and volume in CuNiSiCr FSW joints, as detected by 3D X-ray computed tomography

(ROIs), one located within and the other outside the SZ, were examined to assess the effect of FSW on porosity volume. The tomographic analysis revealed a negligible porosity within the ROI of the SZ, in contrast to the region outside the SZ, which exhibited a porosity degree of 6.77%. Pore morphology was further analyzed using two geometric parameters: the maximum Feret diameter (i.e., the longest dimension of a pore) and the equivalent pore diameter (i.e., the diameter of a sphere with the same volume as the pore), as illustrated in Figs. 9a) and b), respectively. According to the literature [72], large irregular or non-spherical pores are primarily associated with LOF defects (see Fig. 5) as a result of incomplete melting. Conversely, pores with high sphericity are generally attributed to the entrapment of hydrogen gas during solidification [73]. During LPBF, the decomposition of copper oxides can release gas bubbles that may become trapped in the solidifying material, ultimately forming highly spherical pores [69]. The pore count outside the SZ decreases with increasing maximum Feret and equivalent diameters. Most pores exhibit maximum Feret diameter below 250 µm and sphericity values above 0.3. Figure 9b) shows the presence of large pores with equivalent diameters ranging from 200 to 400 µm. Although larger pores (> 1250 µm) are rare, their presence can impair the mechanical performance of the CuNiSiCr alloy. A significant reduction in both the pore number and size was observed after the FSW process. The SZ contains very few pores, with maximum Feret diameters ranging from 100 to 150 µm and sphericity values between 0.4 and 0.5. As shown in Fig. 9b), the equivalent pore diameter within the SZ falls between 50 and 60 µm, demonstrating the effectiveness of FSW in mitigating porosity in AM components.

Similar results have been reported in the literature for aluminum alloys produced via LPBF. For instance, Mirandola et al. [74], in their study on the FSW of AM Scalmalloy®, observed pores outside the SZ with equivalent diameters ranging from 180 to 210 µm, while those within

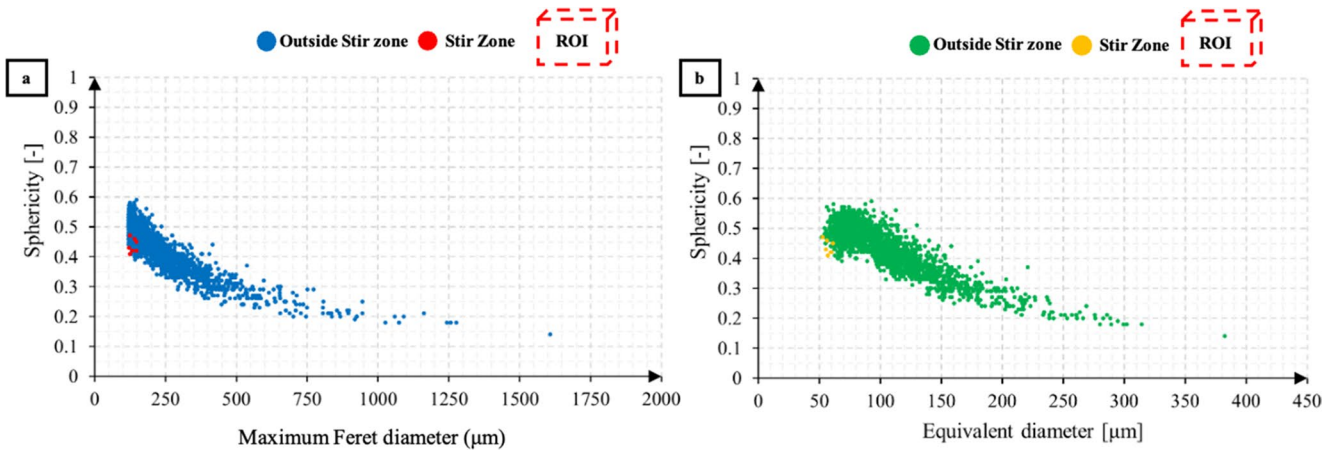

Fig. 9 3D X-ray computed tomography: (**a**) sphericity vs. maximum Feret diameter and (**b**) sphericity vs. equivalent diameter for the two ROIs shown in Fig. 8

the SZ averaged 60 µm. Likewise, Abankar et al. [75], who investigated the FSW of AM A20X, found that the tool stirring action reduced pore sizes from about 180 to 50 µm.

3.3 Heat treatment of the CuNiSiCr as-built and joint samples

Direct aging and solution treatment followed by aging were performed on both the as-built samples and the SZ of the FSW joints to assess the effects of these heat treatments on the microstructure and mechanical properties of CuNiSiCr and its joints. After the solution treatment, the microstructure of CuNiSiCr, Fig. 10a), is characterized by predominantly large grains, often exceeding 100 µm in length and exhibiting a high aspect ratio (i.e., the ratio between the longest and the shortest dimensions). The microstructure also contains a minor fraction of fine grains, only a few micrometers in size. After solution treatment followed by 2 h of aging at 500 °C (corresponding to the condition of maximum hardness achieved during aging, as discussed hereafter and shown in Fig. 11), no significant grain growth occurs, Fig. 10b). This stability is attributed to the relatively low temperature of the aging treatments and the pinning effect exerted by precipitating second phases. Likewise, no grain growth is observed in the as-built CuNiSiCr alloy (Fig. 10c)) and in the FSW joints (Fig. 10d)) after direct aging. Even for prolonged aging times, the microstructures remained stable, showing no evidence of appreciable grain coarsening, Figs. 10e), f), and g).

The hardness values of CuNiSiCr in both the as-built condition and after the solution treatment are comparable, and average around 80–85 HV. This is likely attributable to the as-built microstructure, which was already in a supersaturated solid solution state due to the rapid solidification and cooling of the molten layers during the LPBF process. The extremely high thermal gradient ($\sim 10^6$ K/m) and rapid cooling rates (10^5– 10^6 K/s) widened the solubility limits of alloying elements, promoting the formation of a supersaturated solid solution [61, 76]. In addition, the high thermal conductivity of CuNiSiCr enhanced heat dissipation, further reinforcing this effect. Such a condition is analogous to that produced by solution treatment, where alloying elements were retained in a supersaturated solid solution. In the non-heat-treated condition, the SZ exhibited higher hardness than the as-built material. This improvement is attributed to microstructural refinement and the almost complete absence of porosity, induced by the metal stirring and recrystallization during FSW. Porosity in AM metals typically lowers apparent hardness, as pores act as weak points that collapse under indentation, thereby reducing the metal resistance to deformation. Therefore, the expected hardness of fully dense material should be higher than the recorded values. Aging significantly increased the hardness of CuNiSiCr and its welded joints under all tested conditions. After 1 h of aging, both the SZ and as-built materials showed a marked increase in hardness. The effect was more pronounced after the solution treatment + aging or direct aging (Δhardness ~ 70 HV) than in the welded joints (Δhardness ~ 55 HV). This difference results from the higher concentration of solute atoms retained in a supersaturated solid solution, either as a consequence of the prior solution treatment or of the high cooling rates during the LPBF process. Instead, the recrystallization induced by FSW reduced the concentration of alloying elements in the supersaturated solution state, thereby limiting their strengthening potential during aging. According to Wu et al. [46], the precipitation strengthening of CuNiSiCr is associated with the precipitation of NiSi and Cr_3Si phases. Ageladarakis et al. [77] reported homogeneous precipitation of Ni_2Si in CuNiSi, with sizes ranging from 1 to 10 nm^3 after aging [77], while Lockyer et al. [33] observed δ-Ni_2Si precipitates with average dimensions of 9.30 nm in diameter and 2.84 nm in thickness. Similarly, Cheng et al. [37] identified nanometric Ni_2Si precipitates after aging a CuNiSiCr alloy. As discussed later, it is presumed that similar second-phase precipitates formed during the aging treatments carried out in this study.

When the aging time was extended to 2 h, a further increase of 20–30 HV was observed in both the heat-treated BM and welded joints. As shown in Fig. 11, a peak hardness of 195 HV was achieved in the direct-aged SZ, which was l0–20 HV higher than that of the heat-treated BM. Lockyer and Noble [33] reported a comparable peak hardness of 197 HV for CuNiSi after solution treatment at 800 °C for 2 h followed by 25 h of aging at 450 °C. Notably, the hardness of the solution-treated + aged samples was similar to that of the direct-aged samples. This finding indicates that direct aging alone is sufficient to induce precipitation hardening equivalent to that achieved through conventional solution treatment followed by aging, suggesting that the preliminary solution treatment step is unnecessary for effective precipitation hardening of AM CuNiSiCr. Since the maximum hardness was achieved after aging at 500 °C for 2 h (i.e., peak-aging condition), this setting was selected as the optimal aging condition for further experimentation.

The hardness of the solution-treated and directly aged BM remained relatively stable during prolonged aging, with signs of overaging appearing after 4–8 h. Instead, overaging occurred at shorter times for the directly aged SZ and BM: the former shows signs of overaging after reaching the peak hardness of 195 HV after 2 h, and then gradually decreased to around 180–185 HV.

Figure 12a) and b) show Vickers microhardness maps of a CuNiSiCr joint in the as-welded and after direct aging at the peak conditions, respectively. In the as-welded state, the

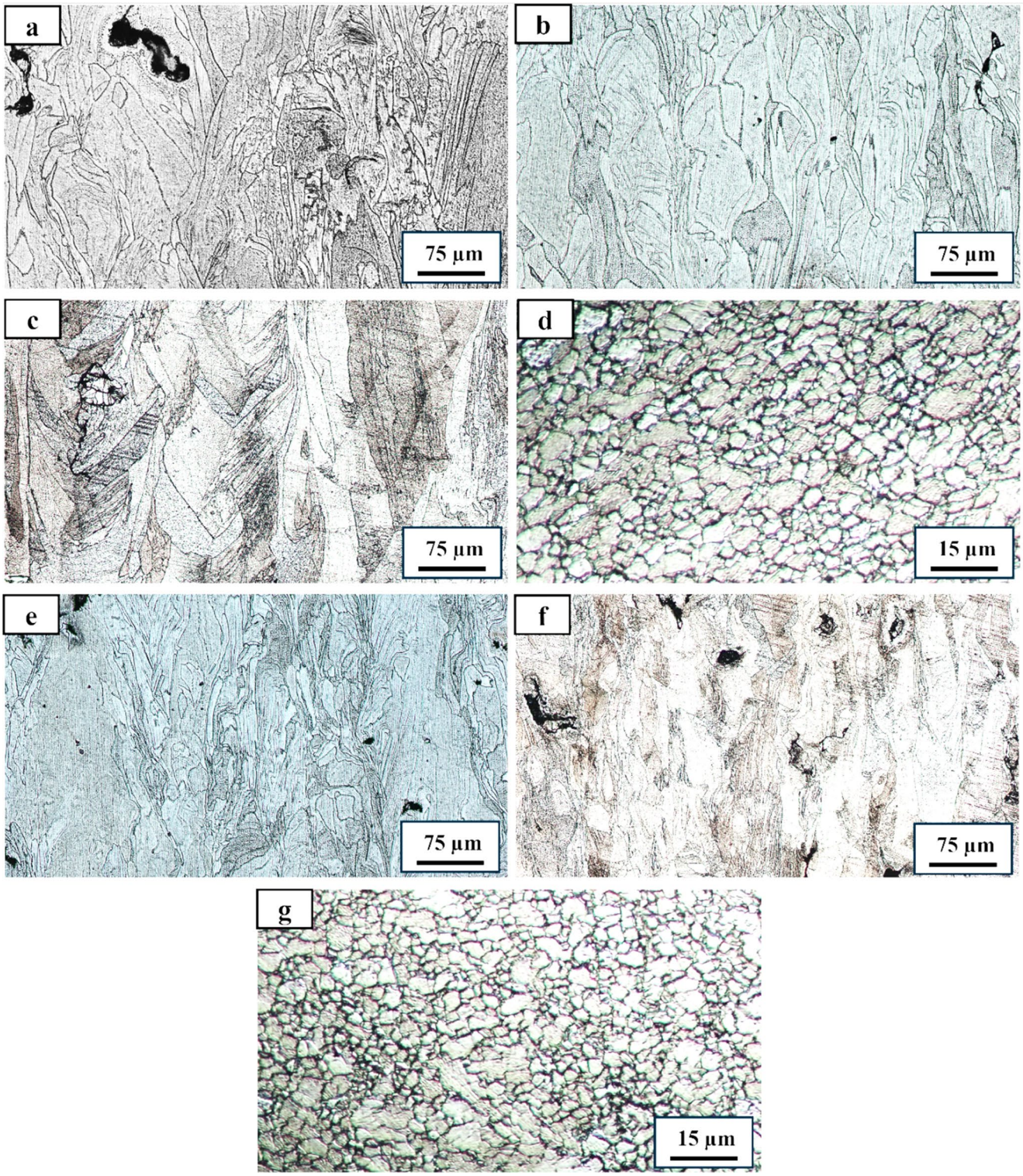

Fig. 10 Optical micrographs of the heat-treated CuNiSiCr alloy under different conditions: (**a**) solution-treated BM, (**b**) solution-treated and peak-aged BM, **(c**) peak direct-aged BM, (**d**) peak direct-aged SZ, (**e**) solution-treated and over-aged BM, (**f**) over-direct-aged BM, (**g**) over-direct-aged SZ

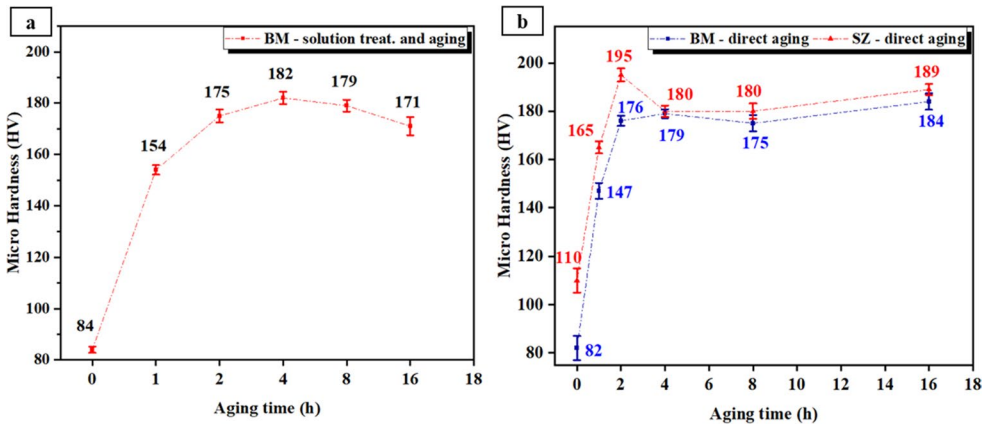

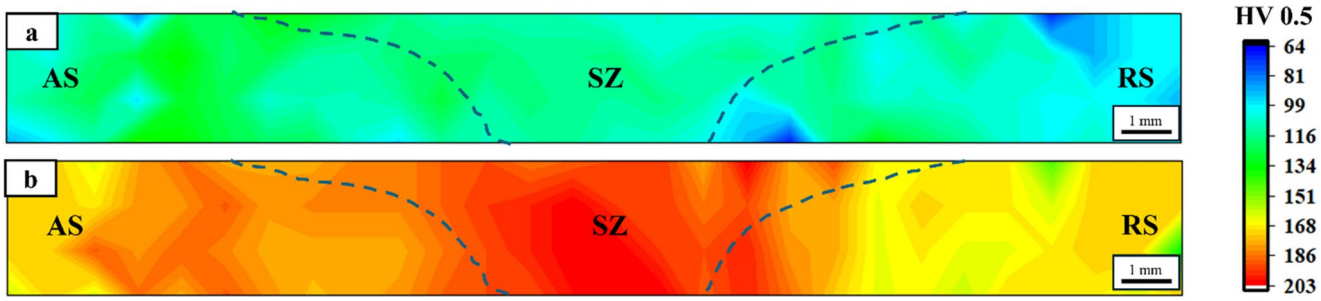

Fig. 11 Microhardness of (**a**) the BM after solution treatment and aging, (**b**) the BM and (**c**) the SZ after direct aging for different times

Fig. 12 Hardness maps of (**a**) an as-welded joint and (**b**) a direct-aged joint of CuNiSiCr

SZ exhibits a nearly uniform hardness distribution ranging from 100 to 125 HV (vs. 80–85 HV for the BM). Similar hardness levels were observed in the HAZ around the joint. Since no appreciable changes in grain size and porosity were detected in this region, the increase in hardness can be primarily attributed to precipitation hardening induced by the heat input during the welding process.

After direct aging, the joints exhibit a marked increase in hardness, particularly in the SZ, where values range from 190 to 205 HV. In contrast, the HAZ shows lower levels of hardness, likely due to the partial aging that had already occurred during the FSW process, reducing the effectiveness of subsequent aging. Moreover, the presence of porosity contributes to the lower apparent hardness and accounts for the greater scatter in hardness values observed outside the SZ, ranging from 160 to 190 HV.

Overall, these findings demonstrate that FSW alone enhances hardness throughout the joint and in its surrounding areas, including the HAZ. Subsequent aging further increases the hardness of the AM CuNiSiCr alloy and its welded joints.

3.4 Structural properties

Figure 13 shows the XRD spectra of the BM, SZ, DA BM, and DA SZ of the CuNiSiCr alloy. As expected, the diffraction patterns reveal the face-centered cubic crystal lattice of the copper matrix, characterized by three prominent peaks corresponding to the (111), (200), and (311) crystallographic planes, as shown in Fig. 13a). No peaks from second phases were detected under any condition, either before or after direct aging. However, nanoscale phases such as NiSi and Cr_3Si could not be detected using standard XRD techniques because they were below the detection limit or present in very low concentrations [33, 78]. A closer examination of the diffraction peaks reveals shifts in the 2θ angles for the different conditions. For instance, Fig. 13b) shows a magnified view of the (111) peak within the 2θ range of 42.75° to 44°, where a noticeable shift is observed for the DA SZ and DA BM samples compared with the BM and SZ. This shift can be explained by considering Bragg's law, as given by Eq. (1):

$$2\,d\,\sin\,\theta\,=\,n\,\lambda \tag{1}$$

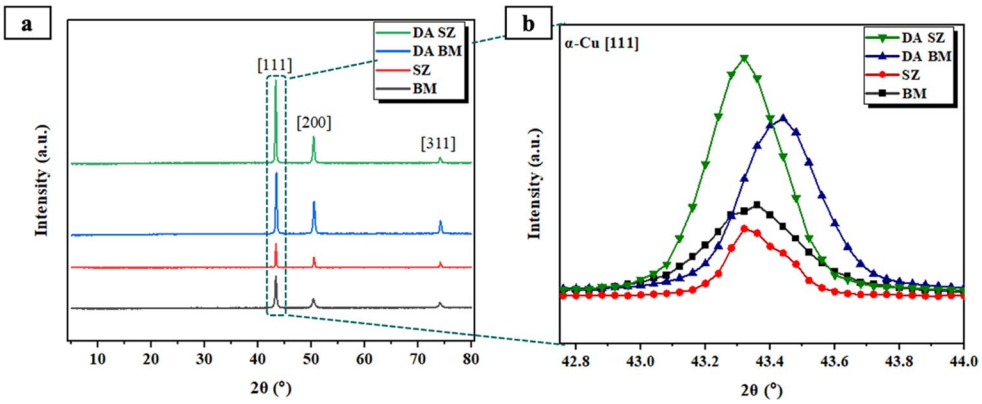

Fig. 13 (**a**) Phase identification from XRD measurements and (**b**) magnified view of the (111) peak shift

where d is the lattice spacing, θ is the diffraction angle, n is a positive integer, and λ is the X-ray wavelength. Assuming a constant wavelength *(λ)*, any shift in θ implies a corresponding change in the lattice spacing *(d)*. Therefore, the observed peak shift suggests a variation in the lattice spacing of the (111) plane for all the DA samples, likely caused by lattice strain induced by the precipitation of second phases such as NiSi and Cr_3Si during aging [33, 62]. The literature [79] has demonstarted that the precipitation of second phases during direct aging can alter the crystal lattice. Conversely, the absence of a noticeable peak shift in the SZ sample compared with the BM suggests that no appreciable phase precipitation occurred during the welding process. The hardness results in Fig. 11 support this interpretation: the SZ exhibited an increase in hardness of about 30 HV, primarily due to the combined effects of grain refinement, reduced porosity, and limited second phase precipitation. In contrast, direct aging led to a much greater hardness increase (85–95 HV at the peak condition), predominantly driven by precipitation strengthening.

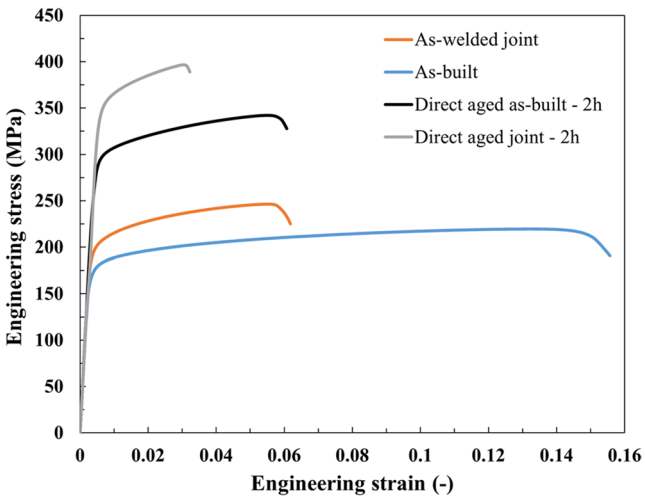

Fig. 14 Stress-strain curves of the CuNiSiCr alloy under different conditions

3.5 Joint tensile strength

Figure 14 displays the stress-strain curves for both the as-built and as-welded CuNiSiCr samples under different conditions. Table 2 summarizes the main mechanical properties and the corresponding fracture locations for each condition. The as-built sample exhibits a YS of 175 ± 10 MPa and UTS of 216 ± 5 MPa, both lower than those measured in the as-welded joints (YS of 205 ± 3 MPa and UTS of 245 ± 15 MPa). This improvement in strength can be attributed to the superior performance of the SZ, which benefited from a minimal porosity (see Figs. 6 and 8) and a refined microstructure (see Fig. 7). In addition, the presence of the HAZ within the gage length contributed to the higher YS, resulting from the partial precipitation strengthening induced during FSW, as confirmed by the corresponding hardness data. However, this gain in strength came at the expense of ductility: 7.3 ± 0.3% for the as-welded condition, compared with 14.2 ± 0.2 for the as-built samples. This reduction in ductility is consistent with previous studies [55, 60, 74]. Both the BM and as-welded samples showed notable improvements in mechanical strength after direct aging at the peak condition. Specifically, YS increased from 175 ± 10 MPa to 290 ± 15 MPa, and UTS from 216 ± 5 MPa to 340 ± 10 MPa. The most pronounced enhancement was observed in the welded joints, consistent with their higher hardness values after aging. Wu et al. [46] reported instead a strength increase of up to 559 MPa in solution-treated and

Table 2 Yield strength (YS), ultimate tensile strength (UTS), and elongation at fracture (e_f %) of the CuNiSiCr alloy under different conditions

Samples	YS (MPa)	UTS (MPa)	e_f %	Failure location
As-built	175±4	216±5	14.2±0.2	B.M.
Direct aged as-built – 2 h	290±15	340±10	6.8±1	B.M.
As-welded joint	205±10	245±15	7.3±0.3	HAZ
Direct aged joint – 2 h	340±5	396±10	3.2±1	HAZ

aged wrought $CuNi_2Si$ alloys, although this was accompanied by an approximately 50% reduction in elongation. Similarly, Lockyer and Noble [33] reported a YS of 610 MPa for wrought Cu-Ni-Si, which was considerably higher than the strength values obtained in this study. This discrepancy can mainly be attributed to the inherent porosity of the LPBF-fabricated CuNiSiCr alloy, which limited the effectiveness of the heat treatments compared with fully dense wrought materials.

In summary, the as-welded joint achieved mechanical efficiencies of 117% in YS, 113% in UTS, and 52% in elongation at fracture compared with the as-built material, indicating a significant enhancement in overall performance. As far as the peak-aged base material is concerned, the corresponding joint retained 117% in YS, 116% in UTS, and 47% in elongation at fracture. These findings underscore the critical role of aging heat treatments in improving the mechanical properties of FSW joints in CuNiSiCr alloys.

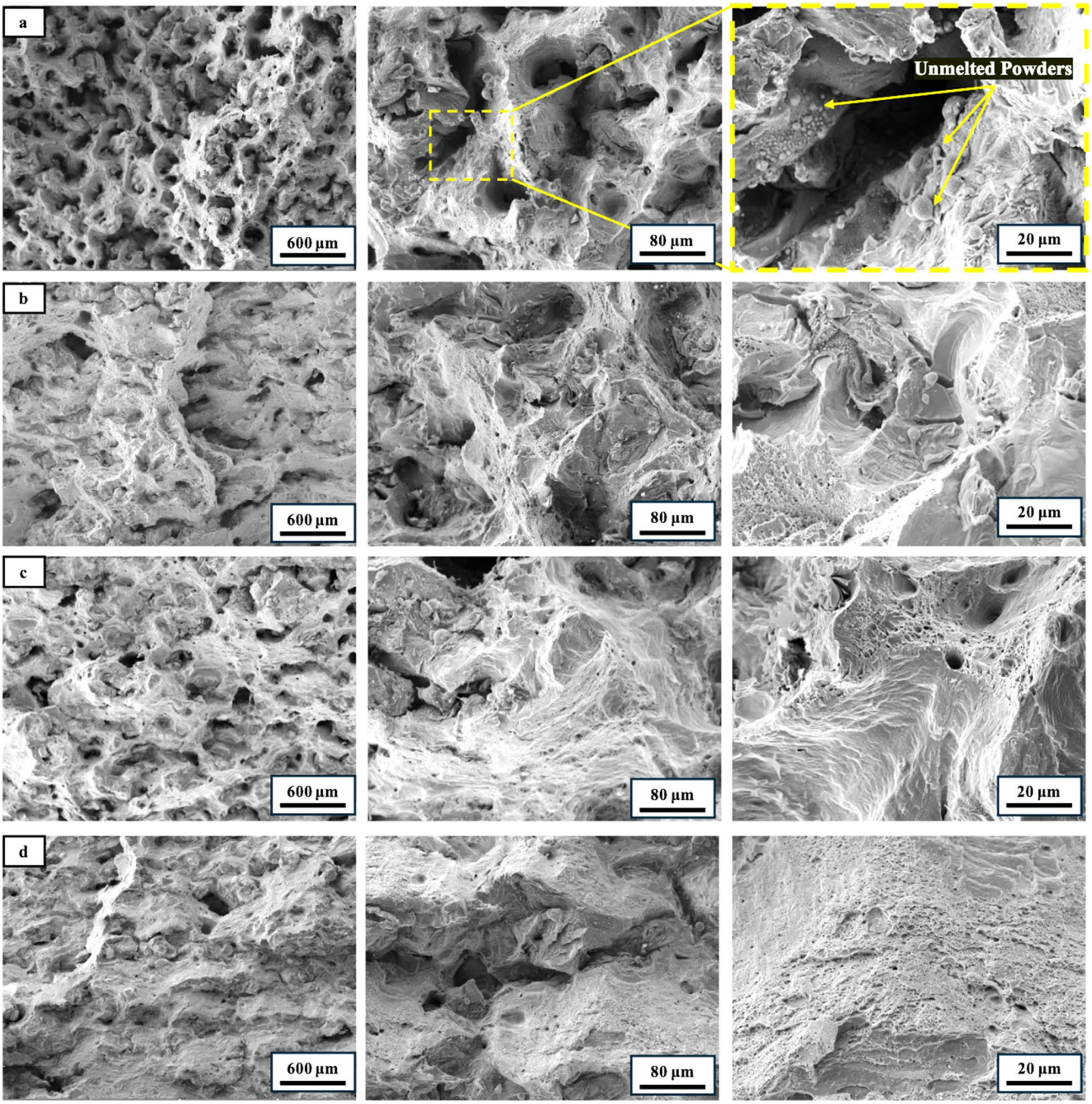

Fig. 15 SEM images of the fractured surfaces of tensile test samples: (**a**) as-built BM, (**b**) peak-aged as-built BM, (**c**) as-welded; and (**d**) peak-aged as-welded conditions

3.6 Fractography

Figure 15 shows the fracture surfaces of the tensile samples, observed at different magnifications, under the examined conditions: (a) as-built BM, (b) peak aged BM, (c) as-welded joint, and (d) peak aged joint. As can be deduced from the fracture locations reported in Table 2, all samples exhibit evidence of porosity on their fracture surfaces, as failure occurred either in the BM or the HAZ. Numerous irregularly shaped pores are distributed throughout the material, giving the fracture surfaces a rough, sponge-like appearance. These pores are surrounded by shallow and fine dimples, typical features of localized plastic deformation and microvoid coalescence, commonly associated with ductile fracture. Under tensile loading, the pores enlarged, promoting crack nucleation and propagation, and ultimately accelerating failure, unlike in fully dense materials [80]. This fracture morphology is particularly pronounced in the BM samples shown in Fig. 15a). In these cases, some of the larger voids also contain unmelted powder, suggesting the presence of LOF defects.

The effects of precipitation strengthening and the associated reduction in ductility are evident in the other sample conditions. The fractographic images of Figs. 15b), c), and d) display similar overall fracture modes but with a less sponge-like texture and a larger number of cleavage facets. This indicates a mixed fracture mechanism, which is primarily brittle, with some ductile features. Such behavior is consistent with the reduced ductility measured during tensile testing of the heat-treated samples. At the microscopic level, the peak-aged joint samples (Fig. 15d)) exhibit the most brittle fracture appearance. Although dimples are still visible under all conditions, they appear smaller and shallower in the peak-aged samples. In addition, features indicative of ductility, such as shear lips, are less evident than in the other conditions, further confirming the transition toward a more brittle fracture behavior in this state.

4 Conclusions

This study investigated the butt FSW of a CuNiSiCr alloy fabricated by LPBF, emphasizing its influence on the porosity, precipitation hardening behavior, and mechanical properties of the joints. Furthermore, the combined effects of FSW and subsequent post-weld heat treatments on the microstructural and mechanical behavior of the welded joints were assessed. The main findings are summarized as follows:

- the metal stirring generated during FSW almost completely eliminated the intrinsic porosity (6.77%vol.) of the LPBF-produced CuNiSiCr alloy, as confirmed by optical microscopy and 3D X-ray computed tomography;
- the intense heat input and resulting recrystallization during FSW led to the formation of very fine grains (average size of ~ 4 μm) in the SZ and induced partial precipitation strengthening in the HAZ. As a result, these regions exhibited higher levels of hardness (up to ~115 HV) compared with the as-built material (~85 HV);
- the hardness of the CuNiSiCr alloy after solution treatment was comparable to that of the as-built condition, presumably due to different mechanisms leading to the retain of alloying elements in a supersaturated solid solution;
- XRD analysis revealed a peak shift of the (111) plane in the aged samples, indicating lattice strain induced by precipitation hardening. In contrast, the absence of a noticeable peak shift for the SZ suggests that no appreciable phase precipitation occurred during the welding process.
- under all heat treatment conditions, maximum hardness was achieved after aging at 500 °C for 2-4 h. The highest value (~195 HV) was measured in the direct-aged SZ, probably due to the combined effects of precipitation hardening and the refined, porosity-free microstructure of this region;
- direct aging produced the greatest increase in tensile strength, reaching about 340 MPa for the as-built samples and about 396 MPa for the joints, compared with 175 MPa for the as-built condition. However, this gain in strength came at the expense of ductility, which dropped to about half that of the as-built samples (elongation at fracture of ~ 7% vs. 14%);
- fractographic analysis revealed that all samples failed under the influence of the intrinsic porosity in the AM CuNiSiCr alloy, while aging promoted a transition toward more brittle fracture modes, consistent with precipitation strengthening and the corresponding loss of ductility.

Overall, these findings demonstrate that FSW combined with direct aging is an effective strategy, comparable to conventional solution treatment followed by aging, for producing joints with balanced strength and ductility, offering a viable route for the fabrication of large and complex AM CuNiSiCr assemblies.

Acknowledgements This study was supported by J-Tech@PoliTO, advanced joining technologies research center at Politecnico di Torino (http://www.j-tech.polito.it/).

Author contributions **M.A.**: Writing – original draft, Methodology, Investigation, Formal analysis, Conceptualization. **V.L.**: Review & editing, Conceptualization. **P.R.S.**: Review & editing, Supervision, Formal analysis, Project administration, Conceptualization.

Funding Open access funding provided by Politecnico di Torino within the CRUI-CARE Agreement. This study was carried out within the Space It Up project funded by the Italian Space Agency, ASI, and the Ministry of University and Research, MUR, under contract n. 2024-5-E.0 - CUP n. I53D24000060005.

Data availability Not applicable.

Code Availability Not applicable.

Declarations

Consent for publication Not applicable.

Ethics approval Not applicable.

Consent to participate Not applicable.

Conflicts of interest/Competing interests The authors declare that they have no known competing financial interests or personal relationships that could have appeared to influence the work reported in this paper.

References

1. Guschlbauer R, Momeni S, Osmanlic F, Körner C (2018) Process development of 99.95% pure copper processed via selective electron beam melting and its mechanical and physical properties. Mater Charact 143:163–170. https://doi.org/10.1016/J.MATCHAR.2018.04.009
2. Mao Z, Zhang DZ, Wei P, Zhang K (2017) Manufacturing feasibility and forming properties of Cu-4Sn in selective laser melting. Materials 10:333. https://doi.org/10.3390/MA10040333
3. Jadhav SD, Dadbakhsh S, Vleugels J, Hofkens J, Puyvelde P, Van, Yang S et al (2019) Influence of Carbon Nanoparticle Addition (and Impurities) on Selective Laser Melting of Pure Copper. Mater. 12:2469. https://doi.org/10.3390/MA12152469
4. Jiang Q, Zhang P, Yu Z, Shi H, Wu D, Yan H et al (2021) A Review on Additive Manufacturing of Pure Copper. Coatings 11:740. https://doi.org/10.3390/COATINGS11060740
5. Colopi M, Demir AG, Caprio L, Previtali B (2019) Limits and solutions in processing pure Cu via selective laser melting using a high-power single-mode fiber laser. Int J Adv Manuf Technol 104:2473–2486. https://doi.org/10.1007/S00170-019-04015-3/FIGURES/12
6. Tran TQ, Chinnappan A, Lee JKY, Loc NH, Tran LT, Wang G et al (2019) 3D Printing of Highly Pure Copper. Met. 2019, Vol 9, Page 756. ;9:756. https://doi.org/10.3390/MET9070756
7. Zeng C, Wen H, Bernard BC, Ding H, Raush JR, Gradl PR et al (2022) Tensile properties of additively manufactured C-18150 copper alloys. Met Mater Int 28:168–180. https://doi.org/10.1007/S12540-021-01052-0
8. Singer F, Deisenroth DC, Hymas DM, Ohadi MM Additively manufactured copper components and composite structures for thermal management applications. Proceedings of the 16th Inter-Society Conference on Thermal and Thermomechanical Phenomena in Electronic Systems, ITherm 2017 2017:174–83. https://doi.org/10.1109/ITHERM.2017.7992469
9. Sciacca G, Sinico M, Cogo G, Bigolaro D, Pepato A, Esposito J (2022) Experimental and numerical characterization of pure copper heat sinks produced by laser powder bed fusion. Mater Des 214:110415. https://doi.org/10.1016/J.MATDES.2022.110415
10. Neugebauer R, Mller B, Gebauer M, Tppel T (2011) Additive manufacturing boosts efficiency of heat transfer components. Assembly Autom 31:344–347. https://doi.org/10.1108/01445151111172925/FULL/PDF
11. Yan X, Chang C, Dong D, Gao S, Ma W, Liu M et al (2020) Microstructure and mechanical properties of pure copper manufactured by selective laser melting. Mater Sci Eng A 789:139615. https://doi.org/10.1016/J.MSEA.2020.139615
12. Martin JD Exploring Additive Manufacturing Processes for Direct 3D Printing of Copper Induction Coils. ASME International Mechanical Engineering Congress and Exposition, Proceedings (IMECE) 2018;2. https://doi.org/10.1115/IMECE2017-71685
13. Constantin L, Wu Z, Li N, Fan L, Silvain JF, Lu YF (2020) Laser 3D printing of complex copper structures. Addit Manuf 35:101268. https://doi.org/10.1016/J.ADDMA.2020.101268
14. Huang J, Yan X, Chang C, Xie Y, Ma W, Huang R et al (2020) Pure copper components fabricated by cold spray (CS) and selective laser melting (SLM) technology. Surf Coat Technol 395:125936. https://doi.org/10.1016/J.SURFCOAT.2020.125936
15. Singh R, Gupta A, Tripathi O, Srivastava S, Singh B, Awasthi A et al (2020) Powder bed fusion process in additive manufacturing: an overview. Mater Today Proc 26:3058–3070. https://doi.org/10.1016/J.MATPR.2020.02.635
16. Gokuldoss PK, Kolla S, Eckert J (2017) Additive manufacturing processes: selective laser melting, electron beam melting and binder jetting—selection guidelines. Materials 10(6):672. https://doi.org/10.3390/MA10060672
17. Wang H, Sen, Chen HG, Gu JW, Hsu CE, Wu CY (2014) Effects of heat treatment processes on the microstructures and properties of powder metallurgy produced Cu–Ni–Si–Cr alloy. Mater Sci Engineering: A 619:221–227. https://doi.org/10.1016/J.MSEA.2014.09.098
18. Srivastava V, Schneider A, … VU-J of M, 2004 undefined. Age-hardening characteristics of Cu–2.4 Ni–0.6 Si alloy produced by the spray forming process. Elsevier n.d
19. Ventura AP, Wade CA, Pawlikowski G, Bayes M, Watanabe M, Misiolek WZ (2017) Mechanical properties and microstructural characterization of Cu-4.3 Pct Sn fabricated by selective laser melting. Metall Mater Trans Phys Metall Mater Sci 48:178–187. https://doi.org/10.1007/S11661-016-3779-X/FIGURES/12
20. Scudino S, Unterdörfer C, Prashanth KG, Attar H, Ellendt N, Uhlenwinkel V et al (2015) Additive manufacturing of Cu–10Sn bronze. Mater Lett 156:202–204. https://doi.org/10.1016/J.MATLET.2015.05.076
21. Mao Z, Zhang DZ, Jiang J, Fu G, Zhang P (2018) Processing optimisation, mechanical properties and microstructural evolution

during selective laser melting of Cu-15Sn high-tin bronze. Mater Sci Eng A 721:125–134. https://doi.org/10.1016/J.MSEA.2018.02.051
22. Zhao C, Wang Z, Li D, Kollo L, Luo Z, Zhang W et al (2021) Selective laser melting of Cu–Ni–Sn: a comprehensive study on the microstructure, mechanical properties, and deformation behavior. Int J Plast 138:102926. https://doi.org/10.1016/J.IJPLAS.2021.102926
23. Yang C, Zhao YJ, Kang LM, Li DD, Zhang WW, Zhang LC (2018) High-strength silicon brass manufactured by selective laser melting. Mater Lett 210:169–172. https://doi.org/10.1016/J.MATLET.2017.09.011
24. Robinson J, Arjunan A, Stanford M, Lyall I, Williams C (2021) Effect of silver addition in copper-silver alloys fabricated by laser powder bed fusion *in situ* alloying. J Alloys Compd 857:157561. https://doi.org/10.1016/J.JALLCOM.2020.157561
25. Liu Y, Zhang J, Tan Q, Yin Y, Liu S, Li M et al (2021) Additive manufacturing of high strength copper alloy with heterogeneous grain structure through laser powder bed fusion. Acta Mater 220:117311. https://doi.org/10.1016/J.ACTAMAT.2021.117311
26. Wallis C, Buchmayr B (2019) Effect of heat treatments on microstructure and properties of CuCrZr produced by laser-powder bed fusion. Mater Sci Eng A 744:215–223. https://doi.org/10.1016/J.MSEA.2018.12.017
27. Ma Z, Zhang K, Ren Z, Zhang DZ, Tao G, Xu H (2020) Selective laser melting of Cu–Cr–Zr copper alloy: parameter optimization, microstructure and mechanical properties. J Alloys Compd 828:154350. https://doi.org/10.1016/J.JALLCOM.2020.154350
28. Zhang DQ, Liu ZH, Li S, Muzzammil M, Wong CH, Chua CK (2014) Selective laser melting: On the studyof microstructure of K220. Proceedings of the International Conference on Progress in Additive Manufacturing. ;0:176–84. https://doi.org/10.3850/978-981-09-0446-3_049
29. Zhou Y, Zeng X, Yang Z, Wu H (2018) Effect of crystallographic textures on thermal anisotropy of selective laser melted Cu-2.4Ni-0.7Si alloy. J Alloys Compd 743:258–261. https://doi.org/10.1016/J.JALLCOM.2018.01.335
30. Mašek J, Koutný D, Popela R Thermal conductivity of Cu7.2Ni1.8Si1Cr copper alloy produced via SLM and ability of thin-wall structure fabrication 2019:119–129. https://doi.org/10.13164/CONF.READ.2018.12
31. Edens WW, Ingerson QF (1979) Of Wis both. Copper-nickel-silicon-chromium alloy having improved electrical conductivity. 110:601
32. Osorio-Galicia R, Gomez-Garcia C, Alcantara MA, Herrera-Vazquez A (2012) Influence of heat treatment and composition variations on microstructure, hardness, and wear resistance of C 18000 copper alloy. ISRN Mech Eng 2012:1–6. https://doi.org/10.5402/2012/248989
33. Lockyer SA, Noble FW (1994) Precipitate structure in a Cu-Ni-Si alloy. J Mater Sci 29:218–226. https://doi.org/10.1007/BF00356596
34. Tiberto D, Klotz UE, Held F, Wolf G (2019) Additive manufacturing of copper alloys: influence of process parameters and alloying elements. Mater Sci Technol 35:969–977. https://doi.org/10.1080/02670836.2019.1600840
35. Davis DJR (2001) ASM specialty Handbook, copper and copper alloys. ASM Handb :133
36. Ventura AP, Marvel CJ, Pawlikowski G, Bayes M, Watanabe M, Vinci RP et al (2017) The effect of aging on the microstructure of selective laser melted Cu-Ni-Si. Metall Mater Trans A 48:6070–6082. https://doi.org/10.1007/S11661-017-4363-8
37. Cheng JY, Tang BB, Yu FX, Shen B (2014) Evaluation of nanoscaled precipitates in a Cu–Ni–Si–Cr alloy during aging. J Alloys Compd 614:189–195. https://doi.org/10.1016/J.JALLCOM.2014.06.089
38. Marques A, Cunha A, Gasik M, Carvalho O, Silva FS, Bartolomeu F 3D multi-material laser powder bed fusion: Ti6Al4V–CuNi2SiCr parts for aerospace applications. Progress Additive Manuf 2023:1–10. https://doi.org/10.1007/S40964-023-00460-5/FIGURES/10
39. Copper (2023) accessed November 16, (CuNi2SiCr) 3D Printing | Get Custom Metal 3D Prints Fast n.d. https://www.protolabs.com/services/3d-printing/direct-metal-laser-sintering/copper/
40. Ban Y, Zhang Y, Jia Y, Tian B, Volinsky AA, Zhang X et al (2020) Effects of cr addition on the constitutive equation and precipitated phases of copper alloy during hot deformation. Mater Des 191:108613. https://doi.org/10.1016/J.MATDES.2020.108613
41. Zhao Z, Xiao Z, Li Z, Qiu W, Jiang H, Lei Q et al (2019) Microstructure and properties of a Cu–Ni–Si–Co–Cr alloy with high strength and high conductivity. Mater Sci Eng A 759:396–403. https://doi.org/10.1016/J.MSEA.2019.05.003
42. Wang W, Kang H, Chen Z, Chen Z, Zou C, Li R et al (2016) Effects of cr and Zr additions on microstructure and properties of Cu-Ni-Si alloys. Mater Sci Eng A 673:378–390. https://doi.org/10.1016/J.MSEA.2016.07.021
43. Chakrabarti DJ, Laughlin DE (1984) The Cr-Cu (Chromium-Copper) system. Bull Alloy Phase Diagrams 5:59–68. https://doi.org/10.1007/BF02868727
44. Hatakeyama M, Okada K, Sunada S (2022) undefined and KS-NM, Effect of dispersion particles and precipitates on the corrosion properties of ODS-Cu, Cu-Cr-Zr and Cu-Cr alloys in Na2SO4 solutions. Elsevier n.d
45. Ban YJ, Zhang Y, Tian B, Song KX, Zhou M, Zhang X et al (2020) EBSD analysis of hot deformation behavior of Cu-Ni-Co-Si-Cr alloy. Mater Charact 169:110656. https://doi.org/10.1016/J.MATCHAR.2020.110656
46. Wu Y, Li Y, Lu J, Tan S, Jiang F, Sun J (2018) Correlations between microstructures and properties of Cu-Ni-Si-Cr alloy. Mater Sci Eng A 731:403–412. https://doi.org/10.1016/J.MSEA.2018.06.075
47. Singh S, Ramakrishna S, Singh R (2017) Material issues in additive manufacturing: a review. J Manuf Process 25:185–200. https://doi.org/10.1016/J.JMAPRO.2016.11.006
48. Mirandola P, Lunetto V, Novel D, Barozzi M, Bellutti P, De Maddis M et al (2023) Strength and microstructure of friction stir welded additively manufactured Scalmalloy® in as-welded and heat-treated conditions. J Manuf Process 97:1–11. https://doi.org/10.1016/J.JMAPRO.2023.04.051
49. Lee WB, Jung SB (2004) The joint properties of copper by friction stir welding. Mater Lett 58:1041–1046. https://doi.org/10.1016/J.MATLET.2003.08.014
50. Rahimzadeh A, Heidarzadeh A, Mohammadzadeh A, Moeini G (2020) Effect of friction stir welding heat input on the microstructure and tensile properties of Cu-Zn alloy containing disordered β phase. J Mater Res Technol 9:11154–11161. https://doi.org/10.1016/J.JMRT.2020.08.010
51. Lader SK, Baruah M, Ballav R, Dutta K, Dwivedi PK, Mudliyar BS (2024) Influence of welding temperature on microstructure and crystallographic texture evolution in the different weld zones of underwater friction stir welding of dissimilar CuZn40 and AA1100-O alloys. Metals Mater Int 31:831–852. https://doi.org/10.1007/S12540-024-01779-6
52. Abdollahzadeh A, Vanani BB, Koohdar H, Jafarian HR (2024) Influence of variation ambient system on dissimilar friction stir welding of Al alloy to Mg alloy by the addition of nanoparticles and interlayer. Metals Mater Int 30:2830–2852. https://doi.org/10.1007/S12540-024-01670-4
53. Ding YX, Wang YQ, Guo S, Xie GM (2024) Effect of rapid cooling on microstructure and mechanical properties in friction stir welded Twin-Induced plasticity steel. Met Mater Int

31:1392–1404. https://doi.org/10.1007/S12540-024-01811-9/FIGURES/13
54. Matilainen VP, Pekkarinen J, Salminen A (2016) Weldability of additive manufactured stainless steel. Phys Procedia 83:808–817. https://doi.org/10.1016/J.PHPRO.2016.08.083
55. Moeini G, Sajadifar SV, Wegener T, Brenne F, Niendorf T, Böhm S (2019) On the low-cycle fatigue behavior of friction stir welded Al–Si12 parts produced by selective laser melting. Mater Sci Eng A 764:138189. https://doi.org/10.1016/J.MSEA.2019.138189
56. Prashanth KG, Damodaram R, Scudino S, Wang Z, Prasad Rao K, Eckert J (2014) Friction welding of Al–12Si parts produced by selective laser melting. Mater Des 57:632–637. https://doi.org/10.1016/J.MATDES.2014.01.026
57. Chen X, Zhang J, Chen X, Cheng X, Huang Z (2018) Electron beam welding of laser additive manufacturing Ti–6.5Al–3.5Mo–1.5Zr–0.3Si titanium alloy thick plate. Vacuum 151:116–121. https://doi.org/10.1016/J.VACUUM.2018.02.011
58. Ascari A, Fortunato A, Liverani E, Gamberoni A, Tomesani L (2016) New possibilities in the fabrication of hybrid components with big dimensions by means of selective laser melting (SLM). Phys Procedia 83:839–846. https://doi.org/10.1016/J.PHPRO.2016.08.087
59. Nahmany M, Rosenthal I, Benishti I, Frage N, Stern A (2015) Electron beam welding of AlSi10Mg workpieces produced by selected laser melting additive manufacturing technology. Addit Manuf 8:63–70. https://doi.org/10.1016/J.ADDMA.2015.08.002
60. Abankar M, Lunetto V, Maddis M, De, Lombardi F, Razza V, Spena PR (2024) Friction stir welding of Laser-powder bed fusion manufactured A20X. Periodica Polytech Mech Eng. https://doi.org/10.3311/PPME.38444
61. Rometsch PA, Zhu Y, Wu X, Huang A (2022) Review of high-strength aluminium alloys for additive manufacturing by laser powder bed fusion. Mater Des 219:110779. https://doi.org/10.1016/J.MATDES.2022.110779
62. Copper-Nickel A (2023) accessed October 24, -Silicon-Chromium Alloy for Mold Tooling | MoldMaking Technology n.d. https://www.moldmakingtechnology.com/articles/a-copper-nickel-silicon-chromium-alloy-for-mold-tooling
63. Deutsches Institut für Normung DIN 50125:2016-12. Testing of metallic materials -. Tensile Test Pieces 2016:17
64. ISO 6507- (2025) 1:2023 - Metallic materials — Vickers hardness test — Part 1: Test method n.d. https://www.iso.org/standard/83898.html
65. Yadav S, Paul CP, Jinoop AN, Rai AK, Bindra KS (2020) Laser directed energy deposition based additive manufacturing of copper: process development and material characterizations. J Manuf Process 58:984–997. https://doi.org/10.1016/J.JMAPRO.2020.09.008
66. Khodashenas H, Mirzadeh H (2022) Post-processing of additively manufactured high-entropy alloys - a review. J Mater Res Technol 21:3795–3814. https://doi.org/10.1016/J.JMRT.2022.11.027
67. Motallebi R, Savaedi Z, Mirzadeh H (2022) Post-processing heat treatment of lightweight magnesium alloys fabricated by additive manufacturing: a review. J Mater Res Technol 20:1873–1892. https://doi.org/10.1016/J.JMRT.2022.07.154
68. De Terris T, Baffie T, Ribière C (2023) Additive manufacturing of pure copper: a review and comparison of physical, microstructural, and mechanical properties of samples manufactured with Laser-Powder bed fusion (L-PBF), electron beam melting (EBM) and metal fused deposition modelling (MFDM) technologies. IntJ Mater Form 16:1–25. https://doi.org/10.1007/S12289-023-01755-2/TABLES/13
69. Roccetti Campagnoli M, Galati M, Saboori A (2021) On the processability of copper components via powder-based additive manufacturing processes: potentials, challenges and feasible solutions. J Manuf Process 72:320–337. https://doi.org/10.1016/J.JMAPRO.2021.10.038
70. Moeini G, Sajadifar SV, Wegener T, Rössler C, Gerber A, Böhm S et al (2021) On the influence of build orientation on properties of friction stir welded Al–Si10Mg parts produced by selective laser melting. J Mater Res Technol 12:1446–1460. https://doi.org/10.1016/J.JMRT.2021.03.101
71. Dewangan SK, Banjare PN, Tripathi MK, Manoj MK (2023) Effect of vertical and horizontal zinc interlayer on material flow, microstructure, and mechanical properties of dissimilar FSW of Al 7075 and Mg AZ31 alloys. Int J Adv Manuf Technol 126:4453–4474. https://doi.org/10.1007/S00170-023-11348-7
72. Tradowsky U, White J, Ward RM, Read N, Reimers W, Attallah MM (2016) Selective laser melting of AlSi10Mg: influence of post-processing on the microstructural and tensile properties development. Mater Des 105:212–222. https://doi.org/10.1016/J.MATDES.2016.05.066
73. Li S, Cai B, Duan R, Tang L, Song Z, White D et al (2022) Synchrotron characterisation of ultra-fine grain TiB2/Al-Cu composite fabricated by laser powder bed fusion. Acta Metallurgica Sinica (English Letters) 35(1):78–92. https://doi.org/10.1007/S40195-021-01317-Y
74. Mirandola P, Novel D, Perini M, Benedetti M, Lombardi F, Lunetto V et al (2024) Microstructures and mechanical properties of friction stir welded additively manufactured Scalmalloy®. Int J Adv Manuf Technol 134:1645–1660. https://doi.org/10.1007/S00170-024-14237-9/FIGURES/19
75. Abankar M, Lunetto V, De Maddis M, Russo Spena P (2024) Friction stir welding of additively manufactured A20X aluminum alloy: welding process, mechanical properties, and microstructure. Int J Adv Manuf Technol. https://doi.org/10.1007/S00170-024-14747-6
76. Mair P, Braun J, Kaserer L, March L, Schimbäck D, Letofsky-Papst I et al (2022) Unique microstructure evolution of a novel Ti-modified Al-Cu alloy processed using laser powder bed fusion. Mater Today Commun 31:103353. https://doi.org/10.1016/J.MTCOMM.2022.103353
77. Ageladarakis PA, O'dowd NP, Webster GA (1999) Tensile and Fracture Toughness Tests of CuNiSi at Room and Cryogenic Temperatures
78. Yin J, Lei Q, Zhou S, Zhang X, Kang J, Agbedor SO et al (2024) Synergistic effects of chemical composition on precipitates, dislocations, and mechanical properties of precipitation-strengthened alloys. Mater Sci Eng A 903:146635. https://doi.org/10.1016/J.MSEA.2024.146635
79. Diao Z, Yang F, wang R, Zhang Y, Chen L, Xiong T et al (2023) Effect of heat treatment on the microstructure and properties of CuCrZr alloy manufactured by wire arc additive manufacturing. J Alloys Compd 967:171786. https://doi.org/10.1016/J.JALLCOM.2023.171786
80. Yao CL, Kang HS, Lee KY, Zhai JG, Shim DS (2022) A study on mechanical properties of CuNi2SiCr layered on nickel–aluminum bronze via directed energy deposition. J Mater Res Technol 18:5337–5361. https://doi.org/10.1016/J.JMRT.2022.04.159